Multiscale modelling of solid oxide cells validated on electrochemical impedance spectra and polarization curves

Giuseppe Sassone, Eduardo da Rosa Silva, Manon Prioux, Maxime Hubert, Bertrand Morel, Aline Léon, Jérôme Laurencin

Multiscale Modelling of Solid Oxide Cells Validated on Electrochemical Impedance Spectra and Polarization Curves

G. Sassone[a], E. Da Rosa Silva[a], M. Prioux[a], M. Hubert[a], B. Morel[a], A. Léon[b], and J. Laurencin[a]

[a] Univ. Grenoble Alpes, CEA-Liten, DTCH, 38000 Grenoble, France
[b] European Institute for Energy Research (EIFER), Emmy-Noether-Strasse 11, 76131 Karlsruhe, Germany

Solid oxide cells (SOCs) are high temperature energy-conversion devices, which have attracted a growing interest in the recent years. Indeed, this technology presents a high efficiency and a good reversibility in fuel cell (SOFC) and electrolysis (SOEC) modes. Nevertheless, SOCs durability is still insufficient due to performance degradation during operation. In this context, a physics-based model has been proposed to investigate the impact of operating conditions on the electrodes reaction mechanisms and cell performance. This multiscale model has been developed considering a typical cell composed of a dense electrolyte in $Y_{0.16}Zr_{0.84}O_{1.92}$ (8YSZ) sandwiched between an oxygen electrode in $La_{0.6}Sr_{0.4}Co_{0.2}Fe_{0.8}O_{3-\delta}$-$Ce_{0.8}Gd_{0.2}O_{2-\delta}$ (LSCF-GDC) and a hydrogen electrode made of Ni-YSZ. The model has been validated on global and local polarizations curves in SOFC and SOEC modes, and electrochemical impedance spectra at the open circuit voltage (OCV). The different contributions arising in the impedance spectra have been identified and discussed.

Introduction

Solid oxide cells (SOCs) are high temperature energy-conversion devices, which have attracted a growing interest in the recent years. In the context of the transition towards fossil-free energy market, this technology offers technical solutions for the development of a clean hydrogen economy. Indeed, the SOCs present a high efficiency and a good reversibility in fuel cell (SOFC) and electrolysis (SOEC) modes. However, their durability is still insufficient due to severe performance degradation related to different phenomena occurring in the cell components (1–4). Therefore, for large-scale commercialization, it is still required to improve the SOCs lifetime by maintaining high performance. For this purpose, it is necessary to better understand the impact of global operating conditions on the local processes taking place in the cell components. Besides, the role of the electrode microstructure on the reaction mechanism is still not precisely understood. From this point of view, the modelling can be an efficient tool to unravel and better analyze all the microscopic processes involved in the cell operation. In this context, a physics-based model has been proposed to investigate the impact of operating conditions on the electrodes reaction mechanisms and cell performance. This model takes into account (i) a 3D representation of the electrode microstructure (5), (ii) a description of the reaction mechanisms in full elementary steps (6, 7) and (iii) the SOC geometry

with the gas flow configuration (8, 9). The validated multiscale model has been used to analyze the cell operation in electrolysis and fuel cell modes. The activated reaction pathways associated with the elementary steps in the active layers have been investigated depending on the position along the cell length. Additionally, the different processes occurring in the cell components, arising in the electrochemical impedance spectra (EIS), have been identified and discussed. In the frame of this work, special attention has been paid to the simulation of the complete cell impedance diagram, since the EIS technique is a powerful tool to analyze the kinetic and transport phenomena, but also to perform a prognosis of degradation for long-term operation (10, 11).

Materials and methods

Cell description

A standard hydrogen electrode-supported cell has been considered for this study. The circular cell has an active area of 9.08 cm². It is composed of a $Y_{0.16}Zr_{0.84}O_{1.92}$ (8YSZ) dense electrolyte (ca. 8 µm) and a Ni-8YSZ fuel electrode functional layer (ca. 25 µm) supported on a thick Ni-3YSZ substrate (ca. 280 µm). The oxygen electrode is a bilayer, which includes a $La_{0.6}Sr_{0.4}Co_{0.2}Fe_{0.8}O_{3-\delta}$-$Ce_{0.8}Gd_{0.2}O_{2-\delta}$ (LSCF-GDC) composite functional layer (ca. 20 µm) and a LSCF current collecting layer (ca. 20 µm). A GDC barrier layer (ca. 3 µm) is added between the electrolyte and the oxygen electrode to limit the reactivity.

Experimental setup

Electrochemical tests have been performed in an in-house test bench, which is described in (12). The cell was placed in a metallic housing inside a furnace. A glass sealant (Schott G018-311) was deposited at the cell periphery to ensure the tightness of the fuel compartment. On both sides, the inlet gas was supplied at the cell center by mass flow controllers (Brooks SLA5850S) according to a radial co-flow configuration. A steam generator operated in saturated vapor conditions delivered the steam to the cell. In order to collect the current at the electrodes surface, a Ni grid (100 meshes·cm^{-2}) and two gold grids (100 meshes·cm^{-2}) were used for the hydrogen and the oxygen electrodes, respectively. Local measurements along the cell radius have been performed thanks to a specific design for the metallic interconnect at the air side, which is detailed in (12). In addition, a mechanical load of 600 g·cm^{-2} was applied on the cell to further decrease the contact resistance.

Experimental protocol

For the experiments, the cell was heated up to 860°C with a heating rate of 1°C·min^{-1} and maintained at this temperature for 90 min to form the glass seal. During this first step, the hydrogen and oxygen electrodes were respectively swept under nitrogen (0.5 Nl·h^{-1}) and air (0.5 Nl·h^{-1}). Subsequently, the temperature was decreased to 800°C for the cermet reduction. For this purpose, the N_2 at the fuel electrode was progressively substituted with H_2 while the flow rates at the two electrodes were gradually increased from 0.5 Nl·h^{-1} to 4 Nl·h^{-1}. The cermet was then maintained in this condition, under pure hydrogen, for 16 h to ensure the full reduction of NiO into Ni. Afterwards, the

electrochemical characterizations were carried out in the operating conditions defined in the next section. At the end of the characterizations, the setup was cooled down to room temperature at a rate of $1°C \cdot min^{-1}$. During this step, a mixture of nitrogen and hydrogen was supplied to the hydrogen electrode to maintain the cermet in its reduced state and avoid Ni re-oxidation.

Electrochemical characterizations

In order to validate the model, electrochemical characterizations were performed considering both polarization curves and impedance spectra. As detailed in (12), polarization curves measured in galvanostatic mode were obtained in SOFC and SOEC modes. The local current densities were measured for three zones at center (i.e. gas inlet), middle and edge (i.e. gas outlet) of the circular cell. The data were acquired at different temperatures (700, 750 and 800 °C) and for various inlet flow rates at the hydrogen electrode (3, 6, 9, and 12 $NmL \cdot min^{-1} \cdot cm^{-2}$). Additionally, EIS at the open circuit voltage (OCV) was measured at 750°C, 10/90 H_2/H_2O, total inlet flow rate of 12 $NmL \cdot min^{-1} \cdot cm^{-2}$ at the hydrogen electrode. The experimental data were acquired using a potentiostat/galvanostat (Autolab PGSTAT-302N) equipped with a frequency response analyzer (FRA) module and a 20 A current booster. The ac current amplitude for the EIS acquisition at OCV was imposed to 100 mA. The raw impedance spectra were collected using the NOVA software and then post-treated with the Zview software (ver. 2.70, Scribner Associates) based on equivalent electric circuit model (EECM) shown in Figure 1. The EECM proposed by (13, 14), consists of a resistance that represents the ohmic resistance (R_s) in series with an inductor element (L) that takes into account the inductance of the wires. Four resistance-constant phase element (R-CPE) were used to fit accurately the different EIS contributions at high frequency (HF), medium (or intermediate) frequency (MF) and low frequency (LF) (Figure 1a). It can be noted that the contribution at high frequency is strongly distorted by the inductance related to the wires. To remove this effect, the impedance spectra were simulated with the equivalent circuit without the inductance as shown in Figure 1b. It can be noticed that several cells were tested with a very limited scattering on the experimental results. For the sake of clarity, the iV curves and EIS diagrams retained for the analysis correspond to the data with the lowest standard deviation.

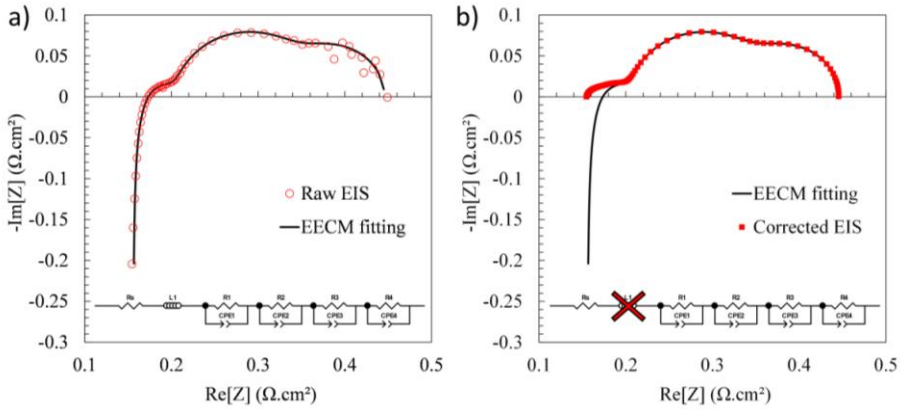

Figure 1. EIS at OCV, 750°C, 10/90 H_2/H_2O, 12 $NmL \cdot min^{-1} \cdot cm^{-2}$ total inlet flow rate, a) comparison between the experimental data and the fitted EIS and b) Simulated EIS without the inductance related to the wires.

Multiscale model description

The multiscale model has been implemented in COMSOL Multiphysics®, MATLAB® and LiveLink™ software. A 2D axisymmetric geometry has been considered thanks to the circular geometry of the cell and the radial co-flow configuration for the experimental setup. In this approach, the set of partial differential equations (PDEs) is solved in the time domain, keeping the full-non linearity of the system. The model is capable of simulating the cell response in different conditions. It is composed of (i) a morphological model to represent the electrodes microstructures; (ii) two electrode-level models based on elementary reactions; and (iii) a cell-level model considering the geometry and the gas distribution to compute all the local quantities (partial pressures, current, etc.) along the cell radius. The microstructural properties coming from the morphological model are used in the electrode-level and cell-level models. For the stationary simulations, as detailed in (12), the apparent exchange current densities used at the macroscopic scale are computed all along the cell length with the electrode models. The stationary model is used for simulating the polarization curves in SOFC and SOEC as presented in (12). This model has been extended to compute the EIS at OCV and under polarization for the complete cell.

The impedance model accounts for the dynamic response of the different irreversible processes arising in the cell layers together with the reversible gas conversion overpotential. For the two electrode models, a transient term has been added in the mass and charge transfer equations for each species considered for the elementary reactions. All the constitutive equations have been already detailed in (6) and (7) for the oxygen and hydrogen electrodes, respectively. It can be noted that the transient terms related to the gas diffusion in the porous electrodes, the solid-state diffusion in the material, the surface diffusion of adsorbed species along with the electronic and ionic currents have been taken into account (6, 7).

The gas conversion contribution in the impedance spectra is induced by the consumption and production of species that modify the gas composition along the cell

length for the two electrodes. In order to consider this contribution in the EIS, the channels distributing the gas over the electrodes are modeled as continuous stirred tank reactors (CSTRs) (6, 15–17). The CSTR model allows computing the boundary conditions in terms of partial pressures that must be applied at the top of the electrode. These boundary conditions are used to simulate the mass transfer within the electrode porous microstructure. For the EIS under polarization, in order to consider the change in composition along the cell radius induced by the reactions, the whole electrode is discretized in *n* annular slices between two radii, *r* and *r+dr*. Therefore, the mass and charge balances in the electrodes associated to the CSTR model for the channels are applied to each slice to calculate the EIS under polarization. For the EIS at OCV, it can be noted that the CSTR is directly computed on the whole electrode, because the composition does not change along the cell radius.

For each slice n of electrode comprised between *r* and *r+dr*, the system of time dependent PDEs related to the processes within the electrode are complemented by equation [1] for the gas channel. It allows computing the molar fraction $y_{\mathrm{i}}(r,t)$ for the i-th species in the channel for the slice *n:*

$$\frac{\mathrm{P_{tot}}\,\mathrm{V_{CSTR}}}{\mathrm{R}\,T}\cdot\frac{\partial y_{\mathrm{i}}(r,t)}{\partial t} = F_{\mathrm{inlet}}\cdot y_{\mathrm{i,inlet}} - F_{\mathrm{outlet}}\cdot y_{\mathrm{i}}(r,t) \pm \left|\vec{J}_{\mathrm{i,n}}(r,t)\right|\cdot \mathrm{A_n} \qquad [1]$$

Where *t* is the time, $\mathrm{P_{tot}}$ is the total pressure (Pa), $\mathrm{V_{CSTR}}$ is the volume of the CSTR (m^3), R is the ideal gas constant ($J{\cdot}mol^{-1}{\cdot}K^{-1}$), T is the operating temperature (K). F_{inlet} and F_{outlet} denote the inlet and outlet total flow rates ($mol{\cdot}s^{-1}$) of the considered slice n while $\mathrm{A_n}$ represents its surface area (m^2). $y_{\mathrm{i,inlet}}$ is the inlet molar fraction for the i-th species. The term $\vec{J}_{\mathrm{i,n}}$ is the molar flow rate across the gas channel/electrode interface ($mol{\cdot}m^{-2}{\cdot}s^{-1}$) for the i-th species at the slice *n* (computed along with the equation of mass transfer in the electrode porosity). In this approach, it is worth noting that F_{inlet}, F_{outlet} and $y_{\mathrm{i,inlet}}$ are assumed to be time independent (6, 18). Their evolution along the cell radius (i.e. for each slice n) is calculated with the stationary model and used as inputs in the dynamic model. In order to compute the impedance of the considered electrode for each slice n, a sinusoidal perturbation is applied on the ionic current in the electrolyte:

$$i(r,t) = i_{\mathrm{dc}}(r) + i_{\mathrm{ac}}(t) \quad \text{with} \quad i_{\mathrm{ac}}(t) = \mathrm{A}\sin(2\pi f t) \qquad [2]$$

Where A and f are respectively the half-amplitude and the frequency for the sinusoid. The dc current $i_{\mathrm{dc}}(r)$ that needs to be applied on each slice comes from the stationary model. Half of the electrolyte thickness is considered in the simulated domain for each slice (at the hydrogen and oxygen sides). The imposed $i(r,t)$ is applied as boundary condition in the electrolyte in such a way that the pure ohmic losses in the dense YSZ are taken into account. The procedure to extract the impedance $Z_{\mathrm{n}}^{\mathrm{O_2}}$ (or $Z_{\mathrm{n}}^{\mathrm{H_2}}$) for each slice at the oxygen (or hydrogen) sides has been already detailed in (19).

For each frequency, the total impedance $Z_{\mathrm{tot}}^{\mathrm{O_2}}$ (or $Z_{\mathrm{tot}}^{\mathrm{H_2}}$) of the whole electrode and half of the electrolyte is calculated knowing that all the local impedances $Z_{\mathrm{n}}^{\mathrm{O_2}}$ (or $Z_{\mathrm{n}}^{\mathrm{H_2}}$) are in a parallel configuration regarding to the current:

$$\frac{1}{Z_{tot}^{k}} = \frac{1}{A_{tot}} \sum_{n=1}^{N} \frac{A_n}{Z_n^k} \quad \text{with} \quad k = O_2 \text{ or } H_2 \qquad [3]$$

Finally, the cell impedance is obtained by the sum of the two contributions:

$$Z_{cell} = Z_{tot}^{O_2} + Z_{tot}^{H_2} \qquad [4]$$

The multiscale model is thus capable of identifying the different contributions related to the different processes in the cell impedance diagram.

Results

Stationary model

The complete validation of the stationary model has been performed on global and local polarization curves. The operating conditions have been explored in terms of cell temperature, SOFC/SOEC operating mode and inlet flow rate at the fuel electrode. All the results have been published elsewhere (12). In Figure 2, a comparison between some experimental and simulated polarization curves is shown as an illustration. It can be seen that the model was able to reproduce the global and local experimental polarization curves. Some deviations were observed approaching the limiting current density, which was mainly ascribed to the uncertainty on the determination of some microstructural properties retrieved from the 3D reconstruction of the Ni-3YSZ support layer (i.e. pore radius and tortuosity factor of the gas phase) (12).

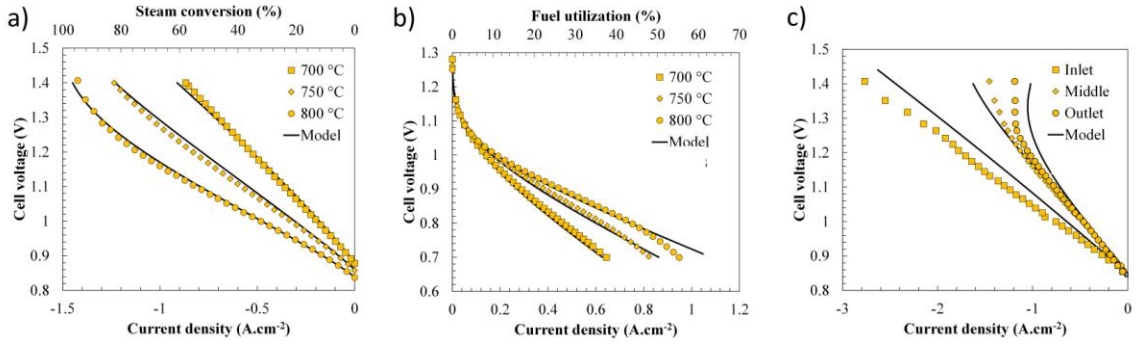

Figure 2. Comparison between the simulation and the experimental data obtained on a standard cell made of the classical Ni-YSZ//YSZ//LSCF-GDC materials: global iV curves in a) SOEC and b) SOFC mode at different temperatures (10/90 H_2/H_2O, Total inlet flow rate=12 $NmL \cdot min^{-1} \cdot cm^{-2}$), c) local iV curves in SOEC mode (800°C, 10/90 H_2/H_2O, Total inlet flow rate=12 $NmL \cdot min^{-1} \cdot cm^{-2}$) (12).

Dynamic model

The validation of the impedance model has been performed on the experimental EIS measured at OCV, 750°C, 10/90 H_2/H_2O, total inlet flow rate 12 NmL·min^{-1}·cm^{-2}, after EECM correction. The EIS diagram has been computed in the same conditions as the experimental EIS, without fitting the model input parameters (the kinetic constants for the reactions and the electrode microstructural parameters are given in (12), while diffusion coefficients, ionic and electronic conductivities along with the double layer capacitances are listed in (6, 7)). As shown in the Nyquist plot (Figure 3a), a good agreement is obtained between experimental and simulated spectra for the contributions at high and low frequencies. However, a higher mismatch in terms of intensity in the imaginary part is observed for the arc at intermediate frequency. The origins of this mismatch is discussed in the next section. It can be also noticed, a frequency lag between the simulation and the experimental data, which is visible in the HF region of the Bode plot (Figure 3b).

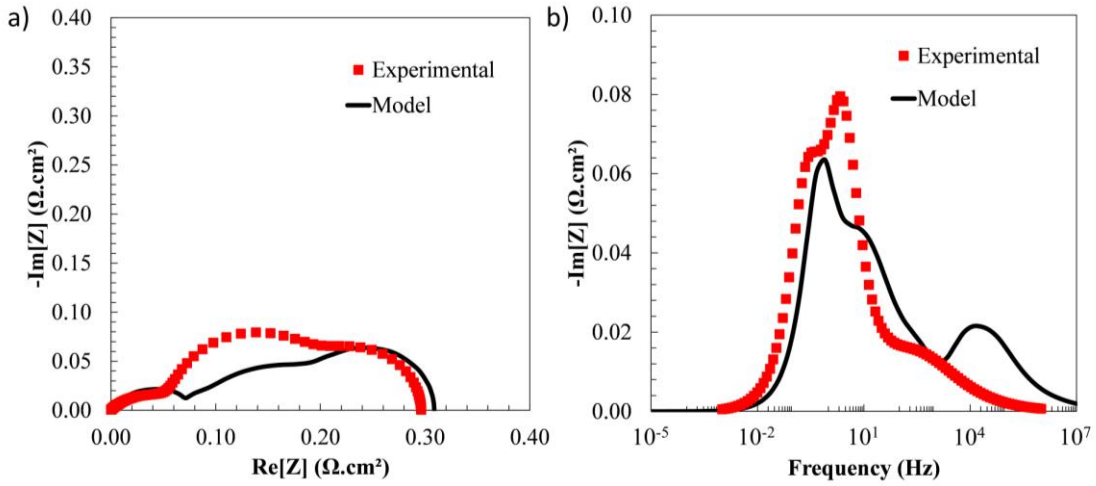

Figure 3. Comparison between simulation and experimental data a) Nyquist and b) Bode plots of the EIS at OCV (750°C, 10/90 H_2/H_2O, total inlet flow rate=12 NmL· min^{-1} · cm^{-2}).The ohmic losses have been removed from the impedance diagrams.

To go further in the model validation, the impact of gas composition on the cell response has been assessed in this study. In Figure 4a, the experimental and simulated polarization resistances (R_p) taken from the EIS at OCV are plotted as a function of the gas composition introduced at the hydrogen electrode (i.e. $p_{H2}/(p_{H2}+ p_{H2O})$ where p_{H2} and p_{H2O} are the hydrogen and steam partial pressures). The evolution of R_p with the gas composition (i.e. $p_{O2}/(p_{O2}+ p_{N2})$) is shown in Figure 4b for the oxygen electrode. In both cases, a rather good agreement is observed between the experimental data and the simulations. Indeed, the model is able to reproduce the dependency of R_p with the gas composition introduced at the two electrodes. Therefore, despite the deviations observed in Figure 3, it can be claimed that the physics-based model can predict quite accurately the cell impedance response at OCV without fitting.

The U-shape of the curve obtained by plotting the R_p evolution with the gas composition has been already discussed in (20). The high R_p values at low hydrogen and steam partial pressures are explained by the depletion in reactants/products, which induces high gas conversion overpotential. Moreover, it can be noticed that the curve is asymmetric, showing a higher R_p at high p_{H2}. This behavior is due to the impact of the hydrogen partial pressure on the electrode activation overpotential related to the complex reaction mechanism in the Ni-YSZ active layer (7). At the oxygen side, the R_p decreases with increasing the oxygen partial pressure. This evolution is explained by both the impact of p_{O2} on the gas conversion overpotential and the activation overpotential associated to the electrochemical processes in the LSCF-GDC electrode (6).

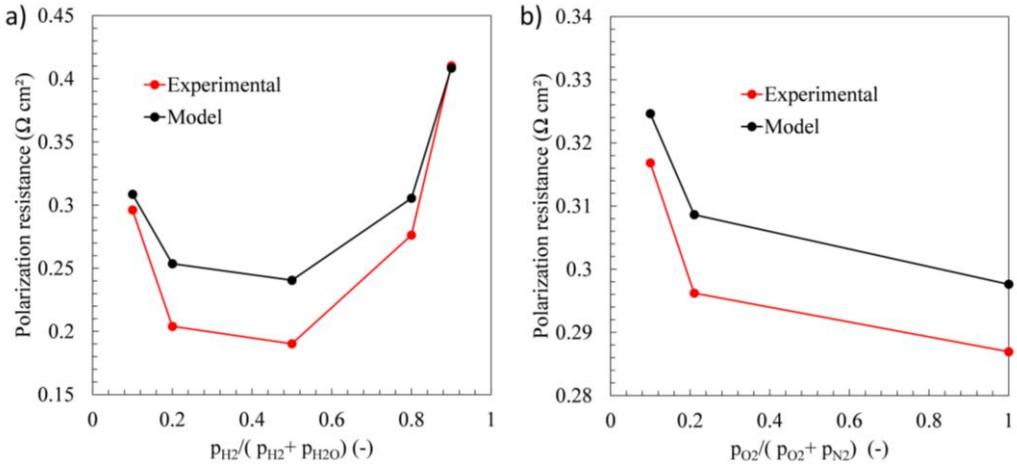

Figure 4. Comparison between simulation and experimental data: R_p measured at OCV and 750°C as function of the a) ratio $p_{H2}/(p_{H2}+ p_{H2O})$ introduced at the hydrogen electrode hydrogen and b) ratio $p_{O2}/(p_{O2}+ p_{N2})$ introduced at the oxygen electrode.

Discussion

Reaction mechanism in the electrodes

It has been found that the physics-based stationary model is able to accurately reproduce the global and local polarization curves in SOFC and SOEC modes (Figure 2). Thus, it can be used to investigate the cell operation and the reaction mechanism depending on the position along the cell radius. As shown in (12), a rather high evolution of current density and gas composition along the cell radius was highlighted with both the model and the experimental setup. Besides, the change in the reaction mechanism was identified by a ratio between two specific kinetic rates. For the hydrogen electrode, it corresponds to the ratio of steam adsorption between YSZ and Ni surfaces. This ratio was found to decrease towards the cell outlet in SOFC mode (12). This means that the adsorption on Ni is more favored compared to YSZ, going towards the cell outlet. This behavior was ascribed to the high coverage of hydroxyl ions, resulting in low available sites on the YSZ surface when the steam partial pressure is increased. The opposite trend was observed in SOEC mode. For the air electrode, the ratio between kinetic rates was related to the incorporation/excorporation (i.e. bulk path) and the direct charge transfer at

the TPBls (i.e. surface path). Such ratio was found to increase towards the cell outlet in SOFC mode (12), meaning that the surface path is promoted at the outlet. This trend was related to the lower concentration of oxygen vacancies in LSCF due to the lower current densities at the cell outlet. Opposite trend was observed in SOEC mode (12). Nevertheless, in both SOEC and SOFC modes, the ratio was higher than the unity ($\zeta > 1$), meaning that the surface path was always dominating over the bulk path.

Contributions in the EIS diagrams at OCV

The stationary model has been also extended to compute the impedance spectra by keeping the full description of the reaction mechanisms in elementary steps. This dynamic model, which is able to compute the impedance diagrams at OCV and under polarization, has been compared to the experimental data at OCV with a reasonable agreement. In such conditions, through a sensitivity analysis, the model can be used to identify and unravel all the different contributions entangled in the Nyquist and Bode plots, as shown in Figure 5. Moving from the lowest to the highest frequency, the first LF contribution is ascribed to the gas conversion (1*) with a characteristic frequency of ca. 0.8 Hz. This order of magnitude for the characteristic frequency for the gas conversion is consistent with the results reported in (15, 17, 21). After that, the main processes involved in the oxygen electrode (2*) take place in the MF range with a characteristic frequency of ca. 13 Hz. This frequency for the oxygen electrode is also coherent with (18, 22). Subsequently, the gas diffusion (3*) in the fuel electrode support layer arises at ca. 390 Hz. This contribution has been identified by studying the impact of the pore size in the Ni-3YSZ support layer on the cell spectrum. The HF arc is mainly attributed to the hydrogen electrode processes (4*) around 10^4 Hz. This result is also consistent with (21, 23). Lastly, the ionic transfer between LSCF and GDC in the oxygen electrode (5*) arises around $6 \cdot 10^4$ Hz, which is convoluted in the hydrogen electrode contribution. These results are in quite good agreement with the model of Bertei et al. (16) and distribution of relaxation time (DRT) study of Wang et al. (24).

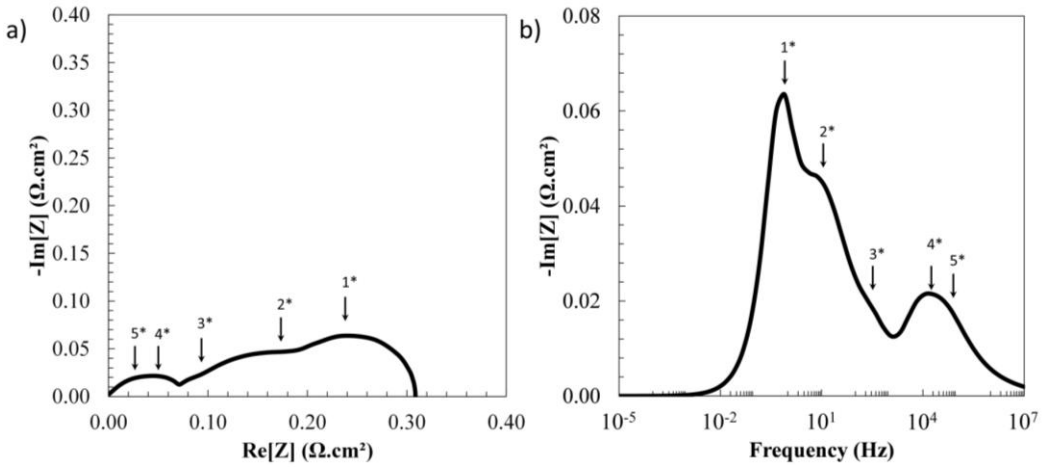

Figure 5. Identification of the processes frequency distribution in the a) Nyquist and b) Bode plots for the simulated EIS at OCV (750°C, 10/90 H_2/H_2O, total inlet flow rate=12 $NmL \cdot min^{-1} \cdot cm^{-2}$).

The identification of the HF and MF contributions to the hydrogen and oxygen electrodes with the model has been confirmed by an experimental sensitivity analysis on the impact of partial pressures on the EIS diagrams. Indeed, the change in the pO2 affects mainly the MF arc in the EIS, with a very slight impact on the HF contribution. On the other hand, as found with the model, the change of pH2 affects the three arcs in the experimental EIS. More in detail, the HF arc increases continuously with the increasing pH2, which is coherent with the aforementioned impact of the pH2 on the hydrogen electrode contribution, as discussed in (7). Concerning the LF arc, the trend is consistent with the U-shape curve shown previously in Figure 4a and the findings of Bessler et al. (20). This result is explained by the gas conversion overpotential. The evolution for the MF arc is related to the gas diffusion in the cermet support.

Impact of gas diffusion contribution on the EIS impedance at OCV

In order to understand the role of the gas diffusion contribution in the fitting of the EIS, a sensitivity analysis was performed on the pore radius of the hydrogen electrode support layer. This parameter has been decreased of an order of magnitude (divided by 10). As shown in Figure 6, the discrepancy between the experimental and simulated impedance spectra at the intermediate frequencies has been significantly reduced. In terms of frequency distribution, in the Bode plot (Figure 6b), the contribution related to the gas diffusion in the cermet substrate becomes strongly convoluted with the oxygen electrode contribution (since the characteristic frequency of the gas diffusion shifts from ca. 390 Hz down to ca. 70 Hz). Therefore, a possible reason behind the discrepancy between the experimental and simulated EIS in the mid-frequency range, shown in Figure 3, can be related to uncertainties in the microstructural properties for the cell substrate (pore radius and tortuosity factor for the gas phase).

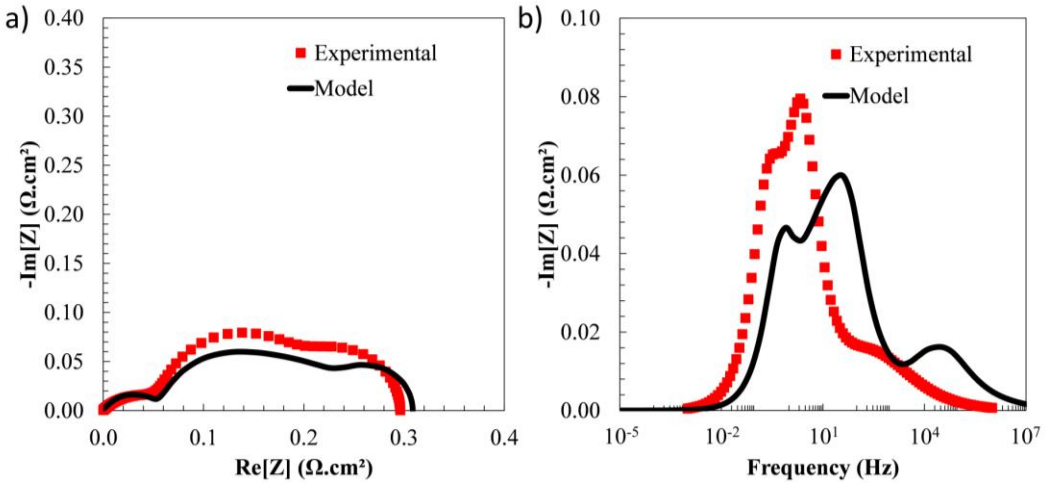

Figure 6. Comparison between normalized simulation and experimental EIS at OCV considering a smaller pore radius for the support layer in the fuel electrode: a) Nyquist and b) Bode plots of the EIS at OCV (750°C, 10/90 H_2/H_2O, total inlet flow rate=12 $NmL \cdot min^{-1} \cdot cm^{-2}$).

Impact of polarization on EIS diagrams

In order to study the impact of polarization on the EIS diagrams, a spectrum has been simulated in SOEC mode at i_{dc}=-0.5 A·cm^{-2} (i.e. SC=32%) and compared to the one computed at OCV in the same conditions (750°C and 12 NmL·min^{-1}·cm^{-2}). As depicted in Figure 7, a substantial swelling of the HF arc can be observed, whereas a shrinkage of the LF contribution is found. The MF arc remains almost constant for the two impedance spectra. These evolutions lead to a decrease in the cell polarization resistance under dc current compared to the one at OCV. The increase of the HF arc, which is related to the hydrogen electrode, is explained by the increase in p_{H2} with increasing the dc current in SOEC mode. This higher p_{H2} causes an increase in the hydrogen electrode polarization resistance, as it has been observed in (7). For the MF arc related to the oxygen electrode, it is worth noting that the high air inlet flow rate limits the change in oxygen partial pressure when the polarization is changed. In this condition, the change in the electrode polarization resistance with the potential is rather limited. Finally, the evolution of the LF contribution associated to the gas conversion is explained by the evolution of the reversible voltage U^{rev} (given by the Nernst equation) with the dc current: at the OCV, the polarization resistance, equal to dU^{rev}/di_{dc}, is rather high and tends to decrease for intermediate currents (before increasing again close to the limiting current).

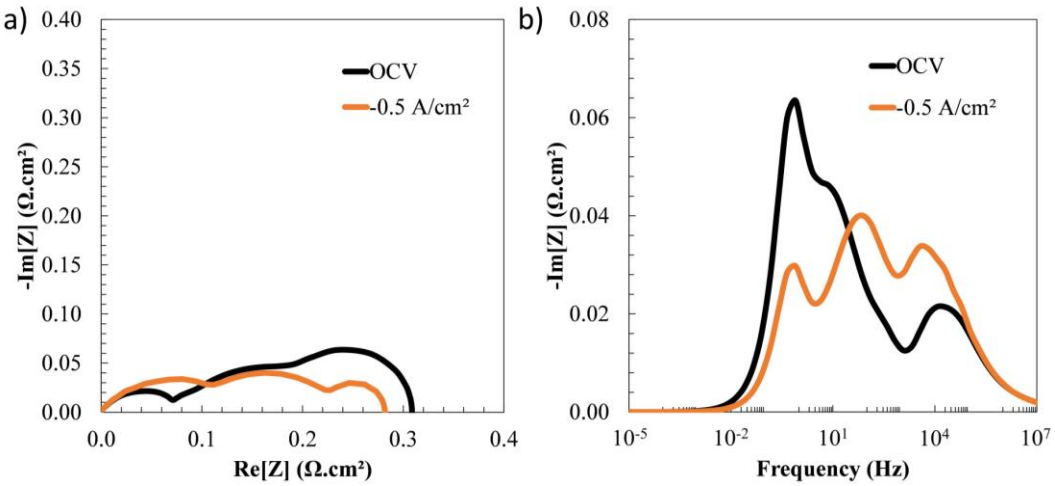

Figure 7. Comparison of the simulated EIS spectra at OCV and under polarization at i_{dc} = -0.5 A·cm^{-2} (750°C, 12 NmL·min^{-1}·cm^{-2}).

Conclusions

A physics-based multiscale model has been developed to compute the cell polarization curves and the EIS at OCV and under dc current. After validation, the model has been used to study the reaction mechanisms in the electrodes along the cell length. The different contributions in the EIS spectra have been identified and discussed. It has been found that the HF arc is mainly related to the hydrogen electrode, whereas the MF arc is related to the oxygen electrode. The contribution due to the gas diffusion in the cermet support layer arises between the responses of the two electrodes. The LF arc is induced by the gas conversion overpotential. It has also been highlighted that the uncertainties in

the microstructure of the cermet substrate can significantly affect the prediction of the EIS diagrams. Finally, the impact of polarization on the spectra has been discussed.

Acknowledgments

The research leading to these results has received funding from Fuel cells and Hydrogen Joint Undertaking under Grant Agreement n◦ 875047 (RUBY Project), grand agreement n◦ 101007175 (REACTT project) and grant agreement n◦ 874577 (NewSOC project). This work has also been supported by Genvia and by the project CELCER-EHT, grant agreement ANR-PEHY-008, France 2030.

References

1. E. Lay-Grindler, J. Laurencin, J. Villanova, P. Cloetens, P. Bleuet, A. Mansuy, J. Mougin, and G. Delette, *Journal of Power Sources*, **269**, 927–936 (2014).
2. M. Trini, A. Hauch, S. De Angelis, X. Tong, P. V. Hendriksen, and M. Chen, *Journal of Power Sources*, **450**, 227599 (2020).
3. F. Wankmüller, J. Szász, J. Joos, V. Wilde, H. Störmer, D. Gerthsen, and E. Ivers-Tiffée, *Journal of Power Sources*, **360**, 399–408 (2017).
4. H. Wang and S. A. Barnett, *J. Electrochem. Soc.*, **165**, F564 (2018).
5. H. Moussaoui, J. Laurencin, Y. Gavet, G. Delette, M. Hubert, P. Cloetens, T. Le Bihan, and J. Debayle, *Computational Materials Science*, **143**, 262–276 (2018).
6. E. Effori, J. Laurencin, E. D. R. Silva, M. Hubert, T. David, M. Petitjean, G. Geneste, L. Dessemond, and E. Siebert, *J. Electrochem. Soc.*, **168**, 044520 (2021).
7. F. Monaco, E. Effori, M. Hubert, E. Siebert, G. Geneste, B. Morel, E. Djurado, D. Montinaro, and J. Laurencin, *Electrochimica Acta*, **389**, 138765 (2021).
8. L. Bernadet, J. Laurencin, G. Roux, D. Montinaro, F. Mauvy, and M. Reytier, *Electrochimica Acta*, **253**, 114–127 (2017).
9. J. Laurencin, D. Kane, G. Delette, J. Deseure, and F. Lefebvre-Joud, *Journal of Power Sources*, **196**, 2080–2093 (2011).
10. A. Donazzi, S. De Pascali, F. Garavaglia, and M. Bracconi, *Electrochimica Acta*, **365**, 137346 (2021).
11. S. B. Beale, M. Andersson, C. Boigues-Muñoz, H. L. Frandsen, Z. Lin, S. J. McPhail, M. Ni, B. Sundén, A. Weber, and A. Z. Weber, *Progress in Energy and Combustion Science*, **85**, 100902 (2021).
12. E. Da Rosa Silva, G. Sassone, M. Prioux, M. Hubert, B. Morel, and J. Laurencin, *Journal of Power Sources*, **556**, 232499 (2023).
13. A. Nechache, A. Mansuy, M. Petitjean, J. Mougin, F. Mauvy, B. A. Boukamp, M. Cassir, and A. Ringuedé, *Electrochimica Acta*, **210**, 596–605 (2016).
14. F. Monaco, D. Ferreira-Sanchez, M. Hubert, B. Morel, D. Montinaro, D. Grolimund, and J. Laurencin, *International Journal of Hydrogen Energy*, **46**, 31533–31549 (2021).

15. S. Primdahl and M. Mogensen, *Journal of The Electrochemical Society*, **145**, 2431–2438 (1998).
16. A. Bertei, G. Arcolini, J. P. Ouweltjes, Z. Wuillemin, P. Piccardo, and C. Nicolella, *Electrochimica Acta*, **208**, 129–141 (2016).
17. W. G. Bessler, *Journal of The Electrochemical Society*, **153**, A1492 (2006).
18. V. Yurkiv, R. Costa, Z. Ilhan, A. Ansar, and W. G. Bessler, *Journal of The Electrochemical Society*, **161**, F480–F492 (2014).
19. M. Hubert, J. Laurencin, P. Cloetens, J. C. da Silva, F. Lefebvre-Joud, P. Bleuet, A. Nakajo, and E. Siebert, *Solid State Ionics*, **294**, 90–107 (2016).
20. W. G. Bessler and S. Gewies, *J. Electrochem. Soc.*, **154**, B548 (2007).
21. P. Caliandro, A. Nakajo, S. Diethelm, and J. Van herle, *Journal of Power Sources*, **436**, 226838 (2019).
22. S. H. Jensen, A. Hauch, P. V. Hendriksen, M. Mogensen, N. Bonanos, and T. Jacobsen, *Journal of The Electrochemical Society*, **154**, B1325 (2007).
23. G. Nusev, B. Morel, J. Mougin, Đ. Juričić, and P. Boškoski, *Journal of Power Sources*, **489** (2021).
24. Y. Wang, N. Xu, E. Dogdibegovic, T. Su, A. D. Brocato, and X.-D. Zhou, *International Journal of Hydrogen Energy*, **47**, 1917–1924 (2022).